Composite Structures 243 (2020) 112214

Contents lists available at ScienceDirect

Composite Structures

journal homepage: www.elsevier.com/locate/compstruct

A new triangular shell element for composites accounting for shear deformation

Imam Jauhari Maknun[a], Irwan Katili[a,*], Adnan Ibrahimbegovic[b], Andi Makarim Katili[a]

[a] Universitas Indonesia, Civil Engineering Department, Depok 16424, Indonesia
[b] Université de Technologie de Compiègne, Sorbonne Universities, CNRS FRE 2012 Roberval, 60203 Compiègne, France

ARTICLE INFO

Keywords:
Composite structures
DKMT18
Naghdi-Reissner-Mindlin shell theory

ABSTRACT

In this paper, we propose an efficient 3-node shell element with 6 DOFs per node based on Naghdi-Reissner-Mindlin theory. This new composite shell element, further denoted as DKMT18, takes into account shear deformation and coupled bending-membrane energy. DKMT18 element passes membrane, bending, and shear patch tests with no spurious mode. It also performs successfully in standard tests for thick and thin shells problems without membrane or shear locking. The proposed shell element is capable of dealing with composite laminated shell structures. The computed results by the DKMT18 element converge more rapidly towards the reference solution compared to any state of-the-art shell element.

1. Introduction

The two basic approaches used to formulate general shell elements are: plate bending and membrane superimposed that leaves two effects uncoupled versus formulations based on three-dimensional continuum mechanics that can take such coupling into account. The first approach of superimposing plate bending and membrane is very simple and can be effective for some applications. For this reason, we rely here on a general continuum mechanics based approach for the shell theory of Naghdi-Reissner-Mindlin [1–7].

The finite element based on such formulation could converge to the exact solution, irrespective of the shell geometry, and adequately accounts for membrane, bending, coupled membrane-bending, and shear effects. For modeling of complex engineering structures, triangular finite elements are frequently used. The triangular shell elements can also more successfully deal with major difficulty in the development of shell finite elements, related to the locking phenomenon for bending dominated shells [8–11].

Locking cure for membrane and shear has been an interesting topic of research. Many different techniques have been proposed. The reduced and selective integration techniques [12–22] are the most straightforward cure that can successfully reduce the numerical locking. However, reduced and selective integration can also result in rank deficiency due to spurious modes. An alternative treatment for locking is the Assumed Natural Strains (ANS) [23–25] method that exhibits better accuracy and robustness. One of the simplest and effective transverse shear formulation is proposed by Hughes and Taylor [26] for a 3-node plate bending element. The more refined ANS is first used for 4-node shell element, referred to as MITC4 (Mixed Interpolation of Tensorial Components), that has been widely used in engineering practice [27].

Lee and Bathe [28] also proposed a 3-node MITC3 shell element, but this element is not free of shear locking. When exact integration is performed, the MITC3 element locks. If one point is used for the evaluation of the shear energy, locking is avoided, but the element has one spurious mode. More recently, the MITC3+ [29] as a new 3-node triangular shell finite element was developed (Lee et al., 2014) to improve the performance of MITC3. Here a cubic bubble function is used for the interpolation of the rotations to enrich the bending displacement fields. Similarly, a new MITC4+ shell element was developed [30] to provide a significantly improved performance in distorted meshes compared to the MITC4 shell element [27].

Our previous work on the subject builds on top of the development of 3-node DKT [31] and 4-node DKQ [32] elements for thin plate using Discrete Shear and Assumed Natural Strains (ANS) methods to eliminate shear strains [10]. DKT and DKQ elements rely on the Reissner-Mindlin plate model and only impose discrete Kirchhoff constraint to eliminate shear effects. The first attempts to include the shear strain with a triangular element, called DST (Discrete Shear Triangular) [33], and with quadrilateral element, called DSQ (Discrete Shear Quadrilateral) [34]. Unfortunately, in the thick plate problem, neither of these pass the patch test. DST-BK was proposed by Batoz and Katili [35]

* Corresponding author.
E-mail address: irwan.katili@eng.ui.ac.id (I. Katili).

https://doi.org/10.1016/j.compstruct.2020.112214
Received 9 November 2019; Received in revised form 11 March 2020; Accepted 12 March 2020
Available online 22 March 2020

to improve the DST element. The formulation uses a free formulation method and incompatible modes. DST-BK element passes the patch tests and gives good results in thin and thick plate problems. Another direction in previous works is the PQI plate element with a set of incompatible modes for bending proposed in [36–38]. In thin plates problems, this element gives similar performance as the DKQ element. Moreover, the element PQI also gives excellent performance in thick plates analysis without using any adjusted parameters. DKMT and DKMQ elements, based on Reissner-Mindlin [6,7] hypothesis, also introduced by Katili [39,40] to analyze thick and thin plate problems. These elements require only C^0 continuity. The applications of DKMQ and DKMT elements in plate and shell problems are presented in [41–54].

The objective of this paper is to build upon our previous works and provide the corresponding extension to composite problems. The proposed element has three nodes and six DOFs per node and is called the DKMT18 element. This new shell element takes into account coupled bending-membrane energy. The DKMT18 element passes the classical patch tests in thick and thin plate problems and provides the solutions converging more quickly towards the reference solutions without shear locking and any spurious modes.

The paper is organized as follows. The kinematic hypothesis for the shell model and the choice of reference frames are explained in Section 2. The formulation of the DKMT18 element is defined in Section 3 with the details of membrane deformation, curvatures strains, and the assumed shear strain field. The stiffness matrix for membrane, bending, and shear for the DKMT18 element, including fictitious stiffness, is defined in Section 4. In Section 5, we present the results of numerical simulation for various isotropic and composite shells, including several classical benchmark tests. Concluding remarks are stated in Section 6.

2. The Naghdi/Reissner-Mindlin shell theory

This section starts with the formulation of Naghdi/Reissner/Mindlin shell theory as a direct extension of the Reissner-Mindlin thick plate theory.

The geometry of the shell is presented in Fig. 1. The position vector $\underset{\sim}{x}_p$is in the middle surface, and the position vector $\underset{\sim}{x}_q$ at an arbitrary point q can be expressed as

$$\underset{\sim}{x}_q(\xi, \eta, z) = \underset{\sim}{x}_p(\xi, \eta) + z\, \underset{\sim}{n}(\xi, \eta) \tag{1}$$

where the normal vector $\underset{\sim}{n}$ of the element is constant in the element.

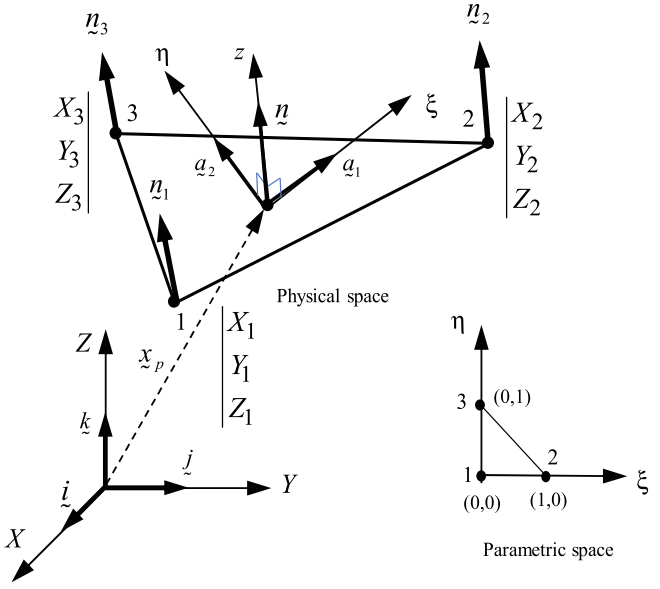

Fig. 1. Geometry of DKMT18 shell element.

Table 1
Linear and quadratic functions.

$N_1 = 1 - \xi - \eta$	$P_4 = 4(1 - \xi - \eta)\xi$
$N_2 = \xi$	$P_5 = 4\xi\eta$
$N_3 = \eta$	$P_6 = 4(1 - \xi - \eta)\eta$

We note in passing that the shell geometry will be interpolated by triangular elements, which allows us to write:

$$\underset{\sim}{x}_q(\xi, \eta, z) = \sum_{i=1}^{3} N_i(\xi, \eta)\, \underset{\sim}{x}_i + z \sum_{i=1}^{3} N_i(\xi, \eta)\, \underset{\sim}{n}_i \tag{2}$$

here $\underset{\sim}{x}_p$ is the position vector at the shell middle surface and $\underset{\sim}{x}_q$ is the position vector along the fiber ($z \neq 0$) orthogonal to the middle surface $\underset{\sim}{n}_i$. The Cartesian coordinate representation of the shell-mid-surface is reconstructed with isoparametric shell element using N_i (ξ, η) are the shape functions (see Table 1) depending on the parametric coordinates (ξ, η) of shell reference element (see Fig. 1).

The isoparametric coordinates allow us to construct more easily the derivative with respect to a local Cartesian basis. Namely, we first define the covariant coordinates by using the natural coordinates of an isoparametric shell element at point p as

$$d\underset{\sim}{x}_p = \begin{Bmatrix} dX \\ dY \\ dZ \end{Bmatrix} = [\underset{\sim}{a}_1 \;\; \underset{\sim}{a}_2] \begin{Bmatrix} d\xi \\ d\eta \end{Bmatrix} \tag{3}$$

where vectors $\underset{\sim}{a}_1$ and $\underset{\sim}{a}_2$ are tangent vectors along ξ and η. Note that $\underset{\sim}{a}_1$ and $\underset{\sim}{a}_2$ are in general not orthogonal, and that they are used to construct the *covariant basis*. Vectors $\underset{\sim}{a}_1$ and $\underset{\sim}{a}_2$ are easily computed by using the isoparametric representation:

$$\begin{aligned} \underset{\sim}{a}_1 &= \underset{\sim}{x}_{p,\xi} = \textstyle\sum_{i=1}^{3} N_{i,\xi}\, \underset{\sim}{x}_i \\ \underset{\sim}{a}_2 &= \underset{\sim}{x}_{p,\eta} = \textstyle\sum_{i=1}^{3} N_{i,\eta}\, \underset{\sim}{x}_i \end{aligned} \tag{4}$$

The local Cartesian basis at $z = 0$, is then written:

$$\begin{aligned} [F_0] &= [\underset{\sim}{a}_1\, \underset{\sim}{a}_2\, \underset{\sim}{n}] \\ \det[F_0] &= (\underset{\sim}{a}_1 \times \underset{\sim}{a}_2).\; \underset{\sim}{n} \\ \underset{\sim}{n} &= \tfrac{\underset{\sim}{a}_1 \times \underset{\sim}{a}_2}{|\underset{\sim}{a}_1 \times \underset{\sim}{a}_2|} \end{aligned} \tag{5}$$

The length ds on the shell surface can be expressed by:

$$(ds)^2 = d\underset{\sim}{x}\,.\; d\underset{\sim}{x} = <d\xi \;\; d\eta>[a] \begin{Bmatrix} d\xi \\ d\eta \end{Bmatrix} \tag{6}$$

where $[a]$ denotes the *metric tensor* in the middle surface. Its coordinate representation is the symmetric, positive-definite matrix, which is defined as:

$$\begin{aligned} [a] &= \begin{bmatrix} a_{11} & a_{12} \\ a_{21} & a_{22} \end{bmatrix} = \begin{bmatrix} \underset{\sim}{a}_1.\, \underset{\sim}{a}_1 & \underset{\sim}{a}_1.\, \underset{\sim}{a}_2 \\ \underset{\sim}{a}_2.\, \underset{\sim}{a}_1 & \underset{\sim}{a}_2.\, \underset{\sim}{a}_2 \end{bmatrix} \\ a &= \det[a]\;;\;\; a_{11} > 0\;;\;\; a_{22} > 0 \\ & \det[a] > 0 \end{aligned} \tag{7}$$

The area of infinitesimal surface element $d\underset{\sim}{A}$ can then be obtained as:

$$\begin{aligned} d\underset{\sim}{A} &= \underset{\sim}{a}_1 d\xi \times \underset{\sim}{a}_2 d\eta \\ d\underset{\sim}{A} &= |\underset{\sim}{a}_1 \times \underset{\sim}{a}_2|\, d\xi\, d\eta\, \underset{\sim}{n} \\ d\underset{\sim}{A} &= \sqrt{a}\; d\xi d\eta\, \underset{\sim}{n} = dA\, \underset{\sim}{n} \end{aligned} \tag{8}$$

$$dA = \sqrt{a}\; d\xi\; d\eta \tag{9}$$

By simple calculations, we further produce the *contravariant* vectors $\underset{\sim}{a}^1$ and $\underset{\sim}{a}^2$, which satisfy the orthogonality relations

$$\underset{\sim}{a}^1.\; \underset{\sim}{a}_1 = \underset{\sim}{a}^2.\; \underset{\sim}{a}_2 = 1 \quad ; \quad \underset{\sim}{a}^1.\; \underset{\sim}{a}_2 = \underset{\sim}{a}^2.\; \underset{\sim}{a}_1 = 0$$

The *contravariant* vectors allow obtaining the inverse matrix $[F_o]^{-1}$, which can be written as

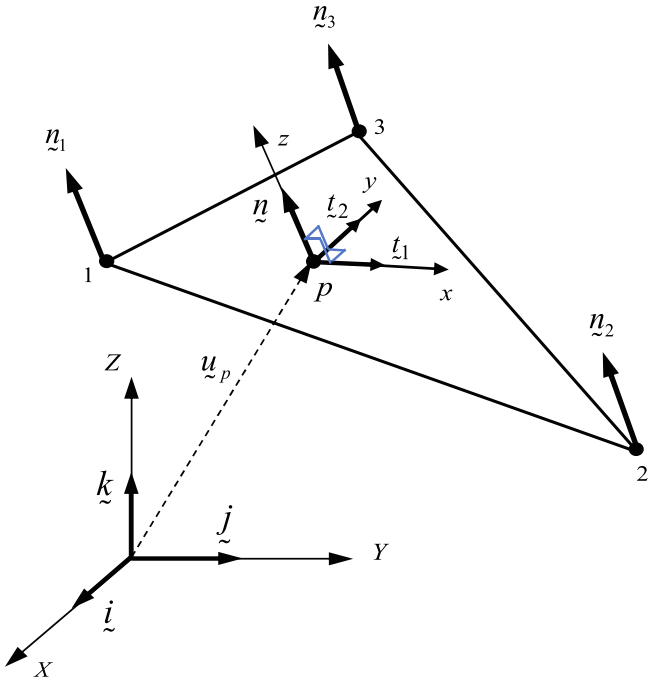

Fig. 2. Local coordinate system *x, y, z,* and global coordinate system *X, Y, Z* at any point *p* at shell mid-surface.

$$[F_0]^{-T} = [\underline{a}^1 \quad \underline{a}^2 \quad \underline{n}]$$
$$[\underline{a}^1 \quad \underline{a}^2] = [\underline{a}_1 \quad \underline{a}_2][a]^{-1} \tag{10}$$

The contravariant base vectors $\underline{a}^1$and$\underline{a}^2$ can be written explicitly as:

$$\underline{a}^1 = \tfrac{1}{a}(a_{22}\,\underline{a}_1 - a_{12}\,\underline{a}_2)$$
$$\underline{a}^2 = \tfrac{1}{a}(-a_{21}\,\underline{a}_1 + a_{11}\,\underline{a}_2) \tag{11}$$

The relationship (3) can now be written in compact notation:

$$\begin{Bmatrix} d\xi \\ d\eta \end{Bmatrix} = \begin{bmatrix} <a^1> \\ <a^2> \end{bmatrix} \begin{Bmatrix} dX \\ dY \\ dZ \end{Bmatrix} \tag{12}$$

The relation of differential calculation between global coordinate and local coordinates system is expressed as (Fig. 2):

$$\begin{Bmatrix} dX \\ dY \\ dZ \end{Bmatrix} = [Q] \begin{Bmatrix} dx \\ dy \\ dz \end{Bmatrix} \tag{13}$$

where:

$$[Q] = [\underline{t}_1 \quad \underline{t}_2 \quad \underline{n}]$$
$$\underline{t}_1 = \underline{n} \times \underline{k}$$
$$\underline{t}_2 = \underline{n} \times \underline{t}_1$$
$$\underline{t}_1 = \underline{i} \quad \text{if} \quad \underline{n} = \pm \underline{k} \tag{14}$$

By combining Eqs. (12) and (13), we can easily obtain the desired derivatives with respect to local Cartesian coordinates, from known values of the derivatives with respect to natural coordinates

$$\begin{Bmatrix} d\xi \\ d\eta \end{Bmatrix} = [C^o] \begin{Bmatrix} dx \\ dy \end{Bmatrix} \text{ and}$$
$$[C^o] = \begin{bmatrix} C^o_{11} & C^o_{12} \\ C^o_{21} & C^o_{22} \end{bmatrix} = \begin{bmatrix} \underline{a}^1 \cdot \underline{t}_1 & \underline{a}^1 \cdot \underline{t}_2 \\ \underline{a}^2 \cdot \underline{t}_1 & \underline{a}^2 \cdot \underline{t}_2 \end{bmatrix} \tag{15}$$

The final results needed pertains to the local cartesian basis at an arbitrary point q ($z \neq 0$). Such local basis, further denoted as $[F_z]$ can be written as:

$$[F_z] = [\underline{a}_{1z} \quad \underline{a}_{2z} \quad \underline{n}] = [F_0] + z[F_n]$$
$$[F_z] = [F_0]([I] + z[b_n]) \tag{16}$$

where $[I]$ as the identity matrix, $[F_n] = [\underline{n}_{,\xi} \quad \underline{n}_{,\eta} \underline{0}]$, whereas $[b_n]$ can be written explicitly as

$$[b_n] = [F_0]^{-1}[F_n] \quad \text{or}$$
$$[b_n] = \begin{bmatrix} b_{n11} & b_{n12} & 0 \\ b_{n21} & b_{n22} & 0 \\ 0 & 0 & 0 \end{bmatrix} = \begin{bmatrix} \underline{a}^1 \cdot \underline{n}_{,\xi} & \underline{a}^1 \cdot \underline{n}_{,\eta} & 0 \\ \underline{a}^2 \cdot \underline{n}_{,\xi} & \underline{a}^2 \cdot \underline{n}_{,\eta} & 0 \\ 0 & 0 & 0 \end{bmatrix} \tag{17}$$

With these results in hand, we can easily write the corresponding strain measures for the strain in a shell model of this kind. The shell membrane strain can be written in matrix notation as

$$\{e\} = \begin{Bmatrix} e_x \\ e_y \\ e_{xy} \end{Bmatrix} = \begin{bmatrix} \underline{t}_1 & 0 \\ 0 & \underline{t}_2 \\ \underline{t}_2 & \underline{t}_1 \end{bmatrix} [C^o]^T \begin{Bmatrix} \underline{u}_{p,\xi} \\ \underline{u}_{p,\eta} \end{Bmatrix} \tag{18}$$

where $\underline{t}_1$ and $\underline{t}_2$ are tangent vectors to shell mid surface, and C^o is defined in Eq. (15).

Assuming that the motion from reference to the deformed configuration of the shell normal is fully described by rotations vector $\underline{\beta}$, which remains independent from displacement field, the shell curvature component can be expressed as

$$\begin{Bmatrix} \chi_x \\ \chi_y \\ \chi_{xy} \end{Bmatrix} = \begin{bmatrix} \underline{t}_1 & 0 \\ 0 & \underline{t}_2 \\ \underline{t}_2 & \underline{t}_1 \end{bmatrix} \left[[bc]^T \begin{Bmatrix} \underline{u}_{p,\xi} \\ \underline{u}_{p,\eta} \end{Bmatrix} + [C^o]^T \begin{Bmatrix} \underline{\beta}_{,\xi} \\ \underline{\beta}_{,\eta} \end{Bmatrix} \right] \tag{19}$$

where

$$[bc] = \begin{bmatrix} bc_{11} & bc_{12} \\ bc_{21} & bc_{22} \end{bmatrix} = [\hat{b}][C^o]$$
$$[\hat{b}] = \begin{bmatrix} b_{n22} & -b_{n12} \\ -b_{n21} & b_{n11} \end{bmatrix}$$
$$[\hat{b}] = \begin{bmatrix} \underline{a}^2 \cdot \underline{n}_{,\eta} & -\underline{a}^1 \cdot \underline{n}_{,\eta} \\ -\underline{a}^2 \cdot \underline{n}_{,\xi} & \underline{a}^1 \cdot \underline{n}_{,\xi} \end{bmatrix} \tag{20}$$

The coefficient $bc_{11} = bc_{12} = bc_{21} = bc_{22} = 0$ when $\underline{n}$ is a constant per element

Finally, the shell shear strain can be written as

$$\{\gamma\} = \begin{Bmatrix} \gamma_x \\ \gamma_y \end{Bmatrix} = [C^o]^T \begin{Bmatrix} \underline{\beta} \cdot \underline{a}_1 + \underline{u}_{p,\xi} \cdot \underline{n} \\ \underline{\beta} \cdot \underline{a}_2 + \underline{u}_{p,\eta} \cdot \underline{n} \end{Bmatrix} \tag{21}$$

where $\underline{\beta}$ is the rotation of the normal vector $\underline{n}$ is orthogonal to the shell surface.

3. Discrete approximation for DKMT18 shell element

The DKMT18 shell element has 18 degrees of freedom, three displacements and three rotations at each node i defined as U_i, V_i, W_i, Θ_{X_i}, Θ_{Y_i}, Θ_{Z_i} (Fig. 3). DKMT18 uses a linear functions for the approximation of displacement in the middle surface, $\underline{u}_p(\xi, \eta)$ and an incomplete quadratic polynomial for the interpolation of rotations $\underline{\beta}(\xi, \eta)$

$$\underline{u}_p(\xi, \eta) = \sum_{i=1}^{3} N_i(\xi, \eta) \begin{Bmatrix} U_i \\ V_i \\ W_i \end{Bmatrix} \tag{22}$$

$$\underline{\beta}(\xi, \eta) = \sum_{i=1}^{3} N_i(\xi, \eta)\, \underline{\beta}_i + \sum_{k=4}^{6} P_k(\xi, \eta)\, \underline{t}_{s_k} \Delta\beta_{s_k} \tag{23}$$

where

$$\underline{\beta}_i = \underline{\Theta}_i \times \underline{n}_i \;\; ; \;\; \underline{t}_{s_k} = \frac{\underline{x}_{ji}}{L_k} \tag{24}$$

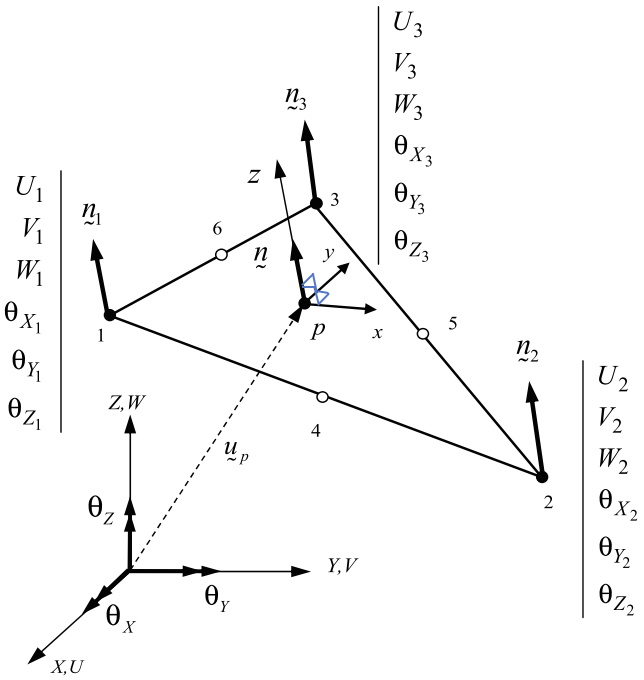

Fig. 3. Nodal degrees of freedom for DKMT18 shell elements.

Substituting (24) into (23), we obtain

$$\underset{\sim}{\beta} = \sum_{i=1}^{3} N_i [RN]_i \begin{Bmatrix} \theta_{Xi} \\ \theta_{Yi} \\ \theta_{Zi} \end{Bmatrix} + \sum_{k=4}^{6} P_k \, \underset{\sim}{t}_{s_k} \Delta\beta_{s_k} \tag{25}$$

$$[RN]_i = [\{RN1\}_i \;\; \{RN2\}_i \;\; \{RN3\}_i]$$
$$[RN]_i = \begin{bmatrix} 0 & n_{Zi} & -n_{Yi} \\ -n_{Zi} & 0 & n_{Xi} \\ n_{Yi} & -n_{Xi} & 0 \end{bmatrix} \tag{26}$$

Here $\Delta\beta_{s_k}(k = 4, 5, 6)$ is a supplementary *dof* at each side of the element (Fig. 4).

Along the side of *i-j*, we have

$$\beta_s = \left(1 - \frac{s}{L_k}\right)\beta_{s_i} + \frac{s}{L_k}\beta_{s_j} + 4\frac{s}{L_k}\left(1 - \frac{s}{L_k}\right)\Delta\beta_{s_k} \tag{27}$$

$$\beta_m = \left(1 - \frac{s}{L_k}\right)\beta_{m_i} + \frac{s}{L_k}\beta_{m_j} \tag{28}$$

where L_k is the length of the side k. The rotation components$\beta_s$and β_m are defined according

$$\beta_s = \underset{\sim}{\beta}\cdot\underset{\sim}{t}_{s_k} \; ; \; \beta_m = \underset{\sim}{\beta}\cdot\underset{\sim}{t}_{m_k}$$
$$\underset{\sim}{t}_{m_k} = \underset{\sim}{t}_{s_k} \wedge \underset{\sim}{n}_k \tag{29}$$

where $\underset{\sim}{t}_{s_k}$and $\underset{\sim}{t}_{m_k}$ $(k = 4, 5, 6)$ are the unit vector tangential and normal to the side of k (Fig. 5).

From (22) and (18), the approximation for membrane strains is

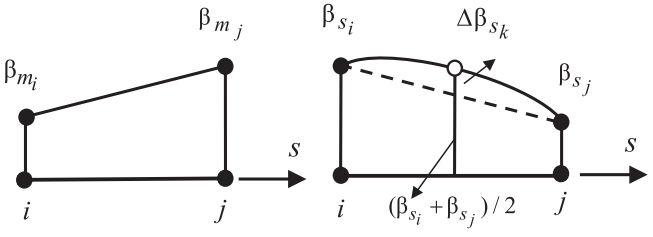

Fig. 4. Variation of rotation β_m and β_s along the sides of DKMT18 shell element.

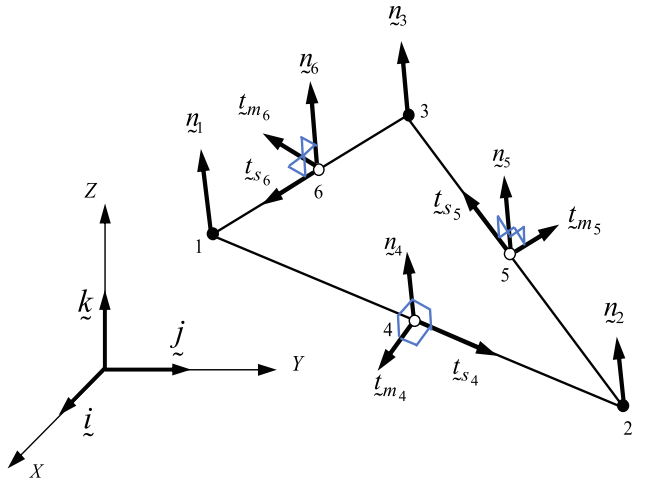

Fig. 5. Normal tangential coordinate system *s-m* with$\underset{\sim}{t}_{s_k}$and $\underset{\sim}{t}_{m_k}$as the unit vector on side *i-j*.

given by:

$$\{e\} = [B_m]\{u_n\} \tag{30}$$

where:

$$[B_m] = [[B_m]^1 \;\; [B_m]^2 \;\; [B_m]^3]$$
$$[B_m]^i = \begin{bmatrix} \langle t_1\rangle N_{i,x} & 0 & 0 & 0 \\ \langle t_2\rangle N_{i,y} & 0 & 0 & 0 \\ \langle t_1\rangle N_{i,y} + \langle t_2\rangle N_{i,x} & 0 & 0 & 0 \end{bmatrix} \tag{31}$$

$$N_{i,x} = N_{i,\xi}C_{11}^o + N_{i,\eta}C_{21}^o$$
$$N_{i,y} = N_{i,\xi}C_{12}^o + N_{i,\eta}C_{22}^o \tag{32}$$

From (22–29) and (19), the discrete approximation for curvature tensor is

$$\{\chi\} = [B_{b_\beta}]\{u_n\} + [B_{b_{\Delta\beta}}]\{\Delta\beta_{s_n}\} \tag{33}$$

$$[B_{b_\beta}] = [[B_{b_{\beta 1}}] \;\; [B_{b_{\beta 2}}] \;\; [B_{b_{\beta 3}}]]$$
$$[B_{b_{\beta i}}] = \begin{bmatrix} <t_1> Nbc1_i & <V1_i> N_{i,x} \\ <t_2> Nbc2_i & <V2_i> N_{i,y} \\ \begin{pmatrix} <t_1> Nbc2_i + \\ <t_2> Nbc1_i \end{pmatrix} & \begin{pmatrix} <V1_i> N_{i,y} + \\ <V2_i> N_{i,x} \end{pmatrix} \end{bmatrix}$$
$$<V_{1i}> = <(\underset{\sim}{t}_1\cdot\underset{\sim}{R}N_{1i})(\underset{\sim}{t}_1\cdot\underset{\sim}{R}N_{2i})(\underset{\sim}{t}_1\cdot\underset{\sim}{R}N_{3i})>$$
$$<V_{2i}> = <(\underset{\sim}{t}_2\cdot\underset{\sim}{R}N_{1i})(\underset{\sim}{t}_2\cdot\underset{\sim}{R}N_{2i})(\underset{\sim}{t}_2\cdot\underset{\sim}{R}N_{3i})>$$
$$Nbc1_i = N_{i,\xi}\, bc_{11} + N_{i,\eta}\, bc_{21}$$
$$Nbc2_i = N_{i,\xi}\, bc_{12} + N_{i,\eta}\, bc_{22} \tag{34}$$

where bc_{11}, bc_{11}, bc_{11}, and bc_{11}, are defined in Eq. (20).

$$[B_{b_{\Delta\beta}}] = \begin{bmatrix} \underset{\sim}{t}_1\cdot\underset{\sim}{t}_{s_k} P_{k,x} & & \\ \cdots & \underset{\sim}{t}_2\cdot\underset{\sim}{t}_{s_k} P_{k,y} & \cdots \\ \underset{\sim}{t}_1\cdot\underset{\sim}{t}_{s_k} P_{k,y} + \underset{\sim}{t}_2\cdot\underset{\sim}{t}_{s_k} P_{k,x} & & \end{bmatrix}_{k=4,6}$$
$$P_{k,x} = P_{k,\xi}C_{11}^o + P_{k,\eta}C_{21}^o$$
$$P_{k,y} = P_{k,\xi}C_{12}^o + P_{k,\eta}C_{22}^o$$
$$<\Delta\beta_{s_n}> = < \Delta\beta_{s_4} \;\; \Delta\beta_{s_5} \;\; \Delta\beta_{s_6} > \tag{35}$$

We next illustrate the proposed manner for dealing with locking in shear in term of assumed shear strains. The assumed shear strain field is assumed constants along each side (Fig. 6) of the element. The corresponding discrete value is first computed in the normal-tangential coordinate system and then transform the resulting expressions to the local coordinate system.

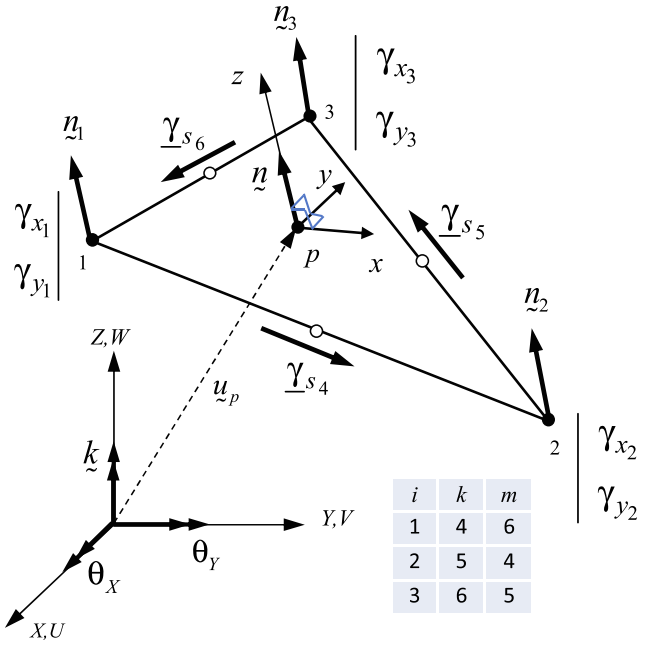

i	k	m
1	4	6
2	5	4
3	6	5

Fig. 6. Constant assumed shear strain on side *i-j*.

$$\{\underset{\sim}{\gamma}\} = \begin{Bmatrix} \underset{\sim}{\gamma}_x \\ \underset{\sim}{\gamma}_y \end{Bmatrix} = \sum_{i=1}^{3} N_i(\xi,\eta) \begin{Bmatrix} \underset{\sim}{\gamma}_{x_i} \\ \underset{\sim}{\gamma}_{y_i} \end{Bmatrix} \tag{36}$$

Shear deformation at node *i*, i.e., $\underset{\sim}{\gamma}_{x_i}$ dan $\underset{\sim}{\gamma}_{y_i}$ can be found by projecting $\underset{\sim}{\gamma}_{s_k}$ on side *k* (Fig. 6) to node *i*

$$\begin{Bmatrix} \underset{\sim}{\gamma}_{s_4} \\ \underset{\sim}{\gamma}_{s_6} \end{Bmatrix} = \begin{bmatrix} C_4 & S_4 \\ C_6 & S_6 \end{bmatrix} \begin{Bmatrix} \underset{\sim}{\gamma}_{x_1} \\ \underset{\sim}{\gamma}_{y_1} \end{Bmatrix}$$
$$\begin{Bmatrix} \underset{\sim}{\gamma}_{s_4} \\ \underset{\sim}{\gamma}_{s_5} \end{Bmatrix} = \begin{bmatrix} C_4 & S_4 \\ C_5 & S_5 \end{bmatrix} \begin{Bmatrix} \underset{\sim}{\gamma}_{x_2} \\ \underset{\sim}{\gamma}_{y_2} \end{Bmatrix}$$
$$\begin{Bmatrix} \underset{\sim}{\gamma}_{s_5} \\ \underset{\sim}{\gamma}_{s_6} \end{Bmatrix} = \begin{bmatrix} C_5 & S_5 \\ C_6 & S_6 \end{bmatrix} \begin{Bmatrix} \underset{\sim}{\gamma}_{x_3} \\ \underset{\sim}{\gamma}_{y_3} \end{Bmatrix} \tag{37}$$

where: $C_k = \underset{\sim}{t}_1 . \underset{\sim}{t}_{s_k}$; $S_k = \underset{\sim}{t}_2 . \underset{\sim}{t}_{s_k}$ (Fig. 6). From (37) above, we further get

$$\begin{Bmatrix} \underset{\sim}{\gamma}_{x_1} \\ \underset{\sim}{\gamma}_{y_1} \\ \underset{\sim}{\gamma}_{x_2} \\ \underset{\sim}{\gamma}_{y_2} \\ \underset{\sim}{\gamma}_{x_3} \\ \underset{\sim}{\gamma}_{y_3} \end{Bmatrix} = \begin{bmatrix} S_6/A_1 & 0 & -S_4/A_1 \\ -C_6/A_1 & 0 & C_4/A_1 \\ -S_5/A_2 & S_4/A_2 & 0 \\ C_5/A_2 & -C_4/A_2 & 0 \\ 0 & -S_6/A_3 & S_5/A_3 \\ 0 & C_6/A_3 & -C_5/A_3 \end{bmatrix} \begin{Bmatrix} \underset{\sim}{\gamma}_{s_4} \\ \underset{\sim}{\gamma}_{s_5} \\ \underset{\sim}{\gamma}_{s_6} \end{Bmatrix} \tag{38}$$

where

$$A_1 = C_4\, S_6 - C_6\, S_4$$
$$A_2 = C_5\, S_4 - C_4\, S_5$$
$$A_3 = C_6\, S_5 - C_5\, S_6 \tag{39}$$

Introducing (38) into (36), we finally have

$$\{\underset{\sim}{\gamma}\} = [B_{s_\gamma}]\{\underset{\sim}{\gamma}_{s_n}\} \tag{40}$$

where

$$[B_{s_\gamma}] = \begin{bmatrix} B_{s_\gamma 11} & B_{s_\gamma 12} & B_{s_\gamma 13} \\ B_{s_\gamma 21} & B_{s_\gamma 22} & B_{s_\gamma 23} \end{bmatrix}$$
$$B_{s_\gamma 11} = \left(\frac{S_6}{A_1}\lambda - \frac{S_5}{A_2}\xi\right) ; B_{s_\gamma 21} = \left(\frac{C_5}{A_2}\xi - \frac{C_6}{A_1}\lambda\right)$$
$$B_{s_\gamma 12} = \left(\frac{S_4}{A_2}\xi - \frac{S_6}{A_3}\eta\right) ; B_{s_\gamma 22} = \left(\frac{C_6}{A_3}\eta - \frac{C_4}{A_2}\xi\right)$$
$$B_{s_\gamma 13} = \left(\frac{S_5}{A_3}\eta - \frac{S_4}{A_1}\lambda\right) ; B_{s_\gamma 23} = \left(\frac{C_4}{A_1}\lambda - \frac{C_5}{A_3}\eta\right) \tag{41}$$

$$\{\underset{\sim}{\gamma}_{s_n}\} = <\underset{\sim}{\gamma}_{s_n}>^T = <\ \underset{\sim}{\gamma}_{s_4}\quad \underset{\sim}{\gamma}_{s_5}\quad \underset{\sim}{\gamma}_{s_6}\ >^T \tag{42}$$

For isotropic material, we can also follow [40,41], to express the assumed independent transverse shear strain $\underset{-s}{\gamma}$ along the side *i-j*

$$\underset{-s}{\gamma} = \frac{D_b}{D_s}\beta_{s,ss} \tag{43}$$

while for composite material we can also follow [46]

$$\underset{-s}{\gamma} = (H^{inv}_{sk21}H_{bk32} + H^{inv}_{sk22}H_{bk22})\beta_{s,ss} \tag{44}$$

where β_s remains the same as previously defined in (27). The assumed independent shear strain $\underset{-s}{\gamma}$ on side-*k* (k = 4, 5, 6) (Fig. 6) is expressed as

$$\underset{-s_k}{\gamma} = -\frac{2}{3}\phi_k \Delta\beta_{s_k} \tag{45}$$

For an isotropic material this lead for this result with

$$\phi_k = \frac{D_b}{D_s}\frac{12}{L_k^2} = \frac{2}{\kappa(1-\upsilon)}\left(\frac{h^2}{L_k^2}\right) \tag{46}$$

and for orthotropic material is

$$\phi_k = (H^{inv}_{sk21}H_{bk32} + H^{inv}_{sk22}H_{bk22})\left(\frac{12}{L_k^2}\right) \tag{47}$$

and:

$$[H_{bk}] = [R_{k_1}]^T[H_b][R_{k_1}]$$
$$[H_{sk}] = [R_{k_2}]^T[H_s][R_{k_2}]$$
$$[H^{inv}_{sk}] = [H_{sk}]^{-1} \tag{48}$$

$$[R_{k_1}] = \begin{bmatrix} S_k^2 & C_k^2 & S_kC_k \\ C_k^2 & S_k^2 & -S_kC_k \\ -2S_kC_k & 2S_kC_k & S_k^2 - C_k^2 \end{bmatrix}$$
$$[R_{k_2}] = \begin{bmatrix} S_k & C_k \\ -C_k & S_k \end{bmatrix} ; \begin{Bmatrix} C_k \\ S_k \end{Bmatrix} = \begin{Bmatrix} \underset{\sim}{t}_1 . \underset{\sim}{t}_{s_k} \\ \underset{\sim}{t}_2 . \underset{\sim}{t}_{s_k} \end{Bmatrix} \tag{49}$$

From Eq. (45) we get

$$\begin{Bmatrix} \underset{\sim}{\gamma}_{s_4} \\ \underset{\sim}{\gamma}_{s_5} \\ \underset{\sim}{\gamma}_{s_6} \end{Bmatrix} = -\frac{2}{3}\begin{bmatrix} \phi_4 & 0 & 0 \\ 0 & \phi_5 & 0 \\ 0 & 0 & \phi_6 \end{bmatrix} \begin{Bmatrix} \Delta\beta_{s_4} \\ \Delta\beta_{s_5} \\ \Delta\beta_{s_6} \end{Bmatrix}$$
$$\{\underset{\sim}{\gamma}_{s_n}\} = [A_\phi]\{\Delta\beta_{s_n}\} \tag{50}$$

Finally, combining (50) and (40) we obtain

$$\{\underset{\sim}{\gamma}\} = \begin{Bmatrix} \underset{\sim}{\gamma}_x \\ \underset{\sim}{\gamma}_y \end{Bmatrix} = [B_{s_\gamma}][A_\phi]\{\Delta\beta_{s_n}\} \tag{51}$$

On each side *i-j*, we recall that $\underset{\sim}{u}_p$ has a linear variation in *s*, as defined in (22), and the rotation $\underset{\sim}{\beta}_s$ has a quadratic variation in *s*, as defined in (27), (see Fig. 4)

$$\gamma_s = \underset{\sim}{u}_{p,s} . \underset{\sim}{n} + \underset{\sim}{\beta} \cdot \underset{\sim}{t}_{s_k} \tag{52}$$

By using variational principal of Hu-Washisu [50,55], we can define:

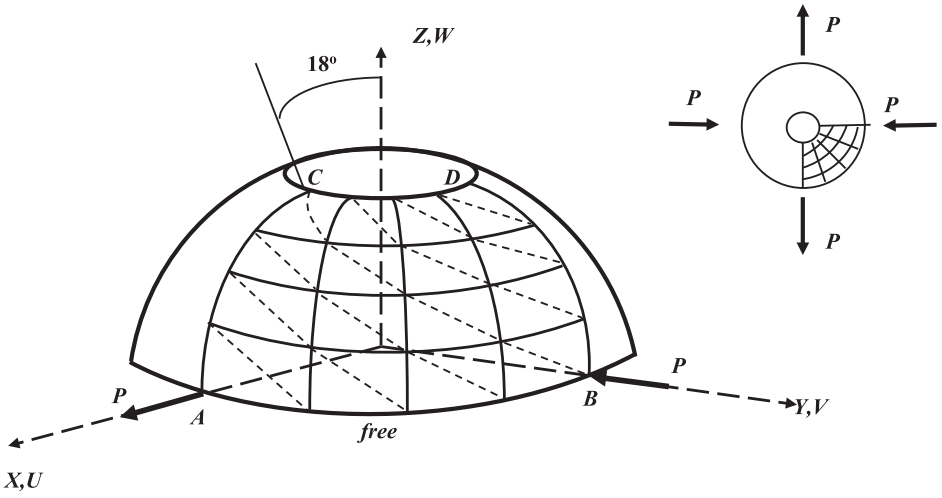

Fig. 7. Hemispherical Shell.

Table 2
Deflection $\underline{U}_A$ ($\underline{U}_A = U_A \times 10^3$) Pinched hemispherical shell.

N	DKMT18	DKMQ24	MITC4
4	95.911	97.935	93.284
8	94.151	94.811	92.848
16	92.806	93.359	92.878
32	92.932	93.372	93.305
64	93.311	93.484	93.517
	REF [57]: 94.000		

$$\underline{\gamma}_{s_k} = \frac{1}{L_k}\int_0^{L_k} \gamma_{s_k}\, ds; \quad k = 4,\ 5,\ 6 \tag{53}$$

Substituting (52) into (53), we obtain

$$\underline{\gamma}_{s_k} = \frac{1}{L_k}\int_0^{L_k} (\underline{u}_{p,s}\cdot\underline{n} + \underline{\beta}\cdot\underline{t}_{s_k})\, ds \tag{54}$$

Substituting (45) into (54) we obtain on each side

$$-\frac{2}{3}\phi_k\Delta\beta_{s_k} = \frac{1}{L_k}\int_0^{L_k} (\underline{u}_{p,s}\cdot\underline{n} + \underline{\beta}\cdot\underline{t}_{s_k})ds \tag{55}$$

where $\underline{n}$ is the unit exterior normal vector on the element. Moreover, from (22) and (27) we get

$$\underline{u}_{p,s} = \tfrac{1}{L_k}(\underline{u}_j - \underline{u}_i)$$
$$\beta_s = \left(1 - \tfrac{s}{L_k}\right)\beta_{s_i} + \tfrac{s}{L_k}\beta_{s_j} + 4\tfrac{s}{L_k}\left(1 - \tfrac{s}{L_k}\right)\Delta\beta_{s_k} \tag{56}$$

Finally, from (55) and (56), we have

$$-\tfrac{2}{3}(1+\phi_k)\Delta\beta_{s_k} = \tfrac{1}{L_k} < n_X \quad n_Y \quad n_Z > \begin{Bmatrix} U_j - U_i \\ V_j - V_i \\ W_j - W_i \end{Bmatrix}$$
$$+ \tfrac{1}{2} < \underline{t}_{s_k}.\, \underline{RN}1_i \ \vdots\ \underline{t}_{s_k}\cdot\underline{RN}2_i \ \vdots\ \underline{t}_{s_k}.\, \underline{RN}3_i > \begin{Bmatrix} \Theta_{Xi} \\ \Theta_{Yi} \\ \Theta_{Zi} \end{Bmatrix} +$$
$$\tfrac{1}{2} < \underline{t}_{s_k}.\, \underline{RN}1_j \ \vdots\ \underline{t}_{s_k}\cdot\underline{RN}2_j \ \vdots\ \underline{t}_{s_k}.\, \underline{RN}3_j > \begin{Bmatrix} \Theta_{Xj} \\ \Theta_{Yj} \\ \Theta_{Zj} \end{Bmatrix} \tag{57}$$

If we applied (57) on all three sides, $\{\Delta\beta_{sn}\}$ becomes a function of degrees of freedom $\{u_n\}$, namely

$$\{\Delta\beta_{s_n}\} = [A_\Delta]^{-1}[A_u]\{u_n\} \tag{58}$$

where:

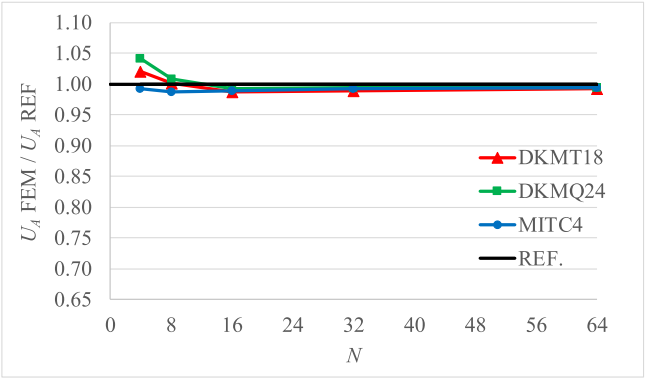

Fig. 8. Convergence of Deflection U_A for the pinched hemispherical shell.

$$[A_\Delta] = -\frac{2}{3}\begin{bmatrix} (1+\phi_4) & 0 & 0 \\ 0 & (1+\phi_5) & 0 \\ 0 & 0 & (1+\phi_6) \end{bmatrix} \tag{59}$$

Substituting (58) into (33) we have

$$\{\chi\} = [B_b(\xi,\eta)]\{u_n\}$$
$$[B_b(\xi,\eta)] = [B_{b_\beta}(\xi,\eta)] + [B_{b_{\Delta\beta}}(\xi,\eta)][A_\Delta]^{-1}[A_u] \tag{60}$$

Substituting (58) into (51) the expression of transversal shear strain deformation, we obtain

$$\{\gamma\} = [B_s(\xi,\eta)]\{u_n\}$$
$$[B_s(\xi,\eta)] = [B_{s_\gamma}(\xi,\eta)][A_{\phi\Delta}][A_u] \tag{61}$$

where:

$$[A_{\phi\Delta}] = [A_\phi][A_\Delta]^{-1} = \begin{bmatrix} \frac{\phi_4}{(1+\phi_4)} & 0 & 0 \\ 0 & \frac{\phi_5}{(1+\phi_5)} & 0 \\ 0 & 0 & \frac{\phi_6}{(1+\phi_6)} \end{bmatrix} \tag{62}$$

4. Stiffness matrix of DKMT18 shell element

In this section, we write the final form of element arrays. The membrane energy is expressed as:

$$\Pi^m_{\text{int}} = \frac{1}{2}\int_A \langle e\rangle[H_m]\{e\}\, dA = \frac{1}{2}\langle u_n\rangle[k_m]\{u_n\} \tag{63}$$

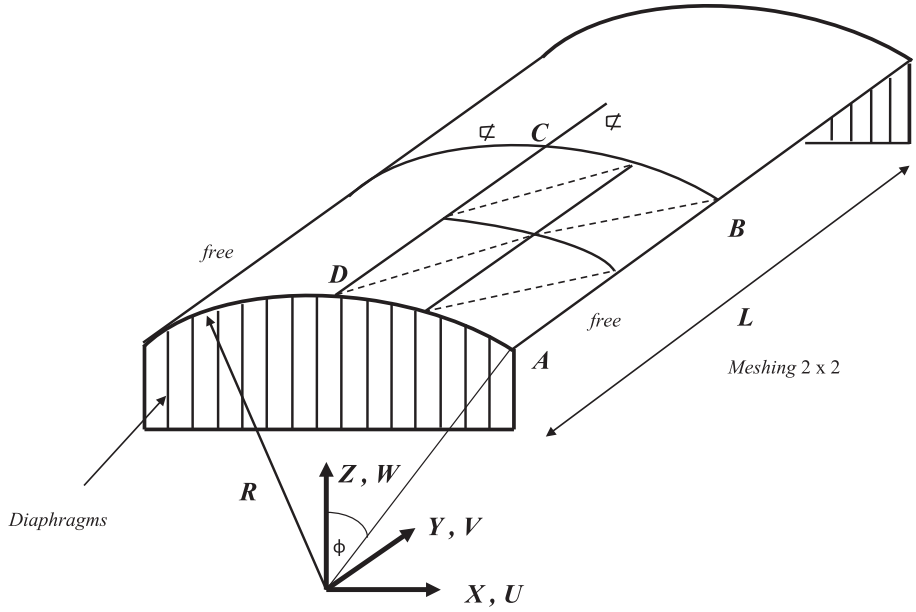

Fig. 9. Scordelis–Lo roof problem.

Table 3
Deflection W_B and W_C.

N	W_B		
	DKMT18	DKMQ24	MITC4
4	−2.665	−3.425	−3.418
8	−3.171	−3.528	−3.539
16	−3.475	−3.585	−3.613
32	−3.573	−3.604	−3.641
64	−3.602	−3.619	−3.650
Deep shell theory REF [58]: −3.610			
Shallow Shell theory REF [58]: −3.703			
N	W_C		
	DKMT18	DKMQ24	MITC4
4	0.394	0.513	0.508
8	0.473	0.529	0.530
16	0.520	0.538	0.543
32	0.536	0.541	0.548
64	0.540	0.544	0.550
Deep Shell REF [58]: 0.541			
Shallow Shell REF [58]: 0.525			

Table 4
Convergence of N_{YB} and M_{XC}.

N	DKMT18		DKMQ24		MITC4	
	N_{YB}	M_{XC}	N_{YB}	M_{XC}	N_{YB}	M_{XC}
4	350.830	1.400	498.43	1.874	496.73	1.808
8	533.490	1.806	592.68	1.998	593.17	1.979
16	609.490	1.984	620.75	2.041	623.12	2.047
32	630.030	2.038	628.28	2.054	631.55	2.068
64	633.710	2.053	631.11	2.061	633.9	2.075
Shallow Shell REF [58]: $N_{YB} = 641.000$; $M_{XC} = 2.056$						

where:

$$[k_m] = \int_A [B_m]^T [H_m] [B_m] \, dA \tag{64}$$

The membrane strain matrix$[B_m]$ for DKMT18 is defined in (31). The bending energy is given by

$$\Pi^b_{\text{int}} = \frac{1}{2} \int_A <\chi> [H_b] \{\chi\} \, dA$$
$$\Pi^b_{\text{int}} = \frac{1}{2} <u_n> [k_b] \{u_n\} \tag{65}$$

with

$$[k_b] = \int_A [B_b]^T [H_b] [B_b] \, dA \tag{66}$$

The bending strain matrix $[B_b]$ for DKMT18 is the same as already defined in (60). The membrane-bending coupling effects energy is given by

$$\Pi^{mb}_{\text{int}} = \frac{1}{2} \int_A <e> [H_{mb}] \{\chi\} \, dA + \frac{1}{2} \int_A <\chi> [H_{mb}] \{e\} \, dA$$
$$\Pi^{mb}_{\text{int}} = \frac{1}{2} <u_n> ([k_{mb}] + [k_{mb}]^T) \{u_n\} \tag{67}$$

with

$$[k_{mb}] = \int_A [B_m]^T [H_{mb}] [B_b] \, dA \tag{68}$$

Finally, transversal shear strain energy is

$$\Pi^s_{\text{int}} = \frac{1}{2} \int_A <\gamma> [H_s] \{\gamma\} \, dA$$
$$\Pi^s_{\text{int}} = \frac{1}{2} <u_n> [k_s] \{u_n\} \tag{69}$$

with

$$[k_s] = \int_A [B_s]^T [H_s] [B_s] \, \text{dA} \tag{70}$$

The shear strain matrix $[B_s]$ for DKMT18 is defined in (61).

The stiffness matrix $[k]$ is the assembly of the stiffness matrices accounting for all contributions due to membrane, bending, coupled membrane-bending and transverse shear:

$$[k] = [k_m] + [k_b] + [k_{mb}] + [k_{mb}]^T + [k_s] \tag{71}$$

The stiffness matrix is determined using the Hammer numerical integration rule. To avoid the danger related to spurious modes, we use a fictitious stiffness.

$$\Pi^{\theta_z}_{\text{int}} = \frac{1}{2} 10^{-3} D_m \int_A (\theta_{z,x} \theta_{z,x} + \theta_{z,y} \theta_{z,y}) dA$$
$$\Pi^{\theta_z}_{\text{int}} = \frac{1}{2} <\theta_n> [k_{\theta_z}] \{\theta_n\} \tag{72}$$

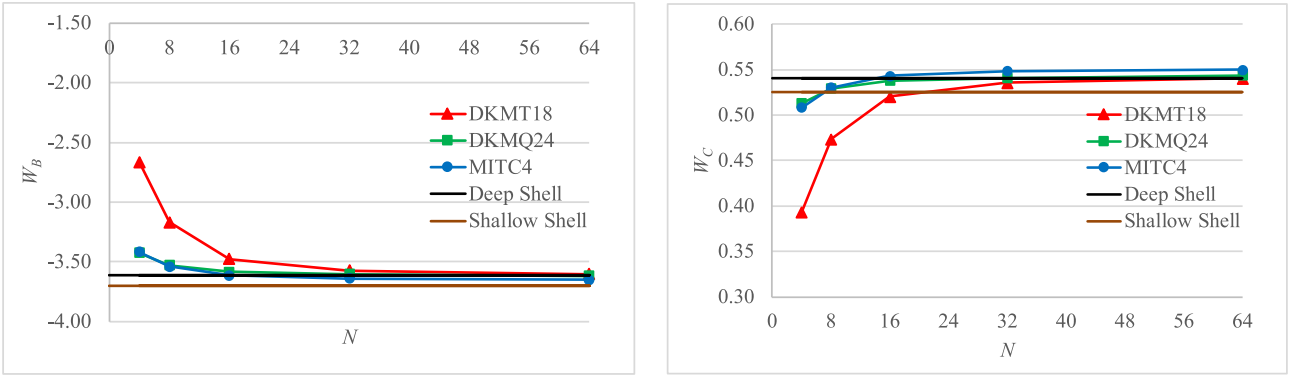

Fig. 10. Convergence of deflection W_B and W_C.

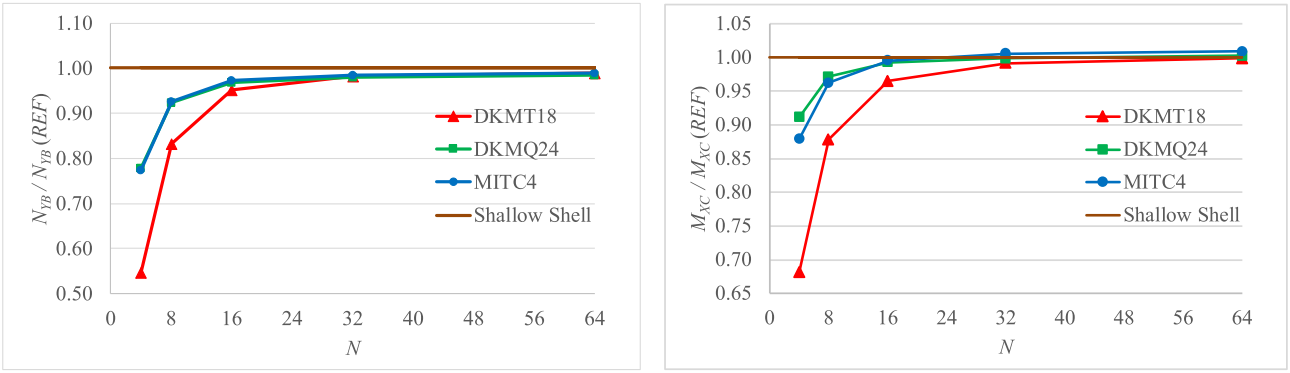

Fig. 11. Convergence of N_{YB} and M_{XC} for the Scordelis–Lo roof problem.

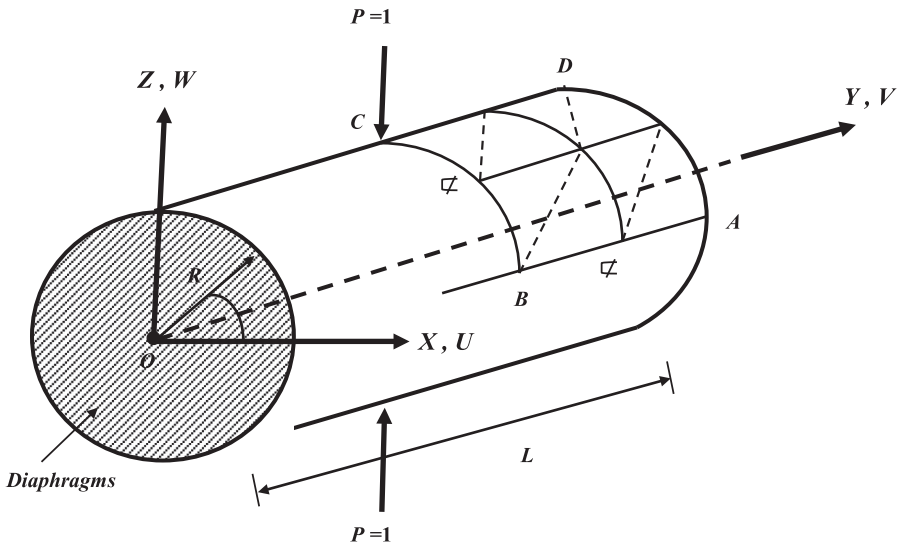

Fig. 12. Pinched cylindrical shell with end diaphragms.

$$\theta_z(\xi,\eta) = \sum_{i=1}^{3} N_i(\xi,\eta) < n_i > \{\theta_n\}$$

$$\theta_z(\xi,\eta) = \sum_{i=1}^{3} < N > < n_{X_i} \quad n_{Y_i} \quad n_{Z_i} > \begin{Bmatrix} \theta_{X_i} \\ \theta_{Y_i} \\ \theta_{Z_i} \end{Bmatrix} \tag{73}$$

$$\begin{Bmatrix} \theta_{z,x} \\ \theta_{z,y} \end{Bmatrix} = [C^o]^T \begin{Bmatrix} \theta_{z,\xi} \\ \theta_{z,\eta} \end{Bmatrix} \tag{74}$$

The size of Matrix $[k_{\theta z}]$ is expanded from (9 × 9) into (18 × 18) to adjust the nodal variables in the element stiffness matrix. The stabilization of fictitious stiffness proposed by *MacNeal* [47,50,56]. We define

$$\Pi_{\text{int}}^{\bar{\theta}_z} = \frac{1}{2} 10^{-3} D_m \int_A (\bar{\theta}_z \cdot \bar{\theta}_z)\, dA = \frac{1}{2} < u_n > [k_{\bar{\theta}_z}] \{u_n\} \tag{75}$$

where we used a small arbitrary factor of stabilization of 10^{-3} that will not affect the results but will enable us to avoid singularities. The final form of the stiffness matrix is:

$$[k] = [k_m] + [k_b] + [k_s] + [k_{\theta_z}] + [k_{\bar{\theta}_z}] \tag{76}$$

With the addition of fictitious stiffness into (71), the spurious modes

Table 5
Deflection $\underline{W_C}$ of Pinched cylindrical shell.

N	$R/h = 100$		
	DKMT18	DKMQ24	MITC4
4	−81.1652	−101.295	−60.957
8	−142.093	−155.214	−122.094
16	−160.795	−167.391	−152.586
32	−164.766	−167.571	−155.214
64	−166.514	−167.589	−157.158
REF [59]	−164.240		
N	$R/h = 10$		
	DKMT18	DKMQ24	MITC4
4	−9.616	−9.426	−10.301
8	−9.679	−10.392	−10.962
16	−9.576	−11.041	−11.540
32	−9.564	−11.897	−11.640
64	−9.555	−12.528	−11.727
REF [61]	−11.351		

will vanish, and we obtained six rigid body motion per element stiffness in (76).

5. Numerical simulations

We first present the validation test introduced for isotropic material by *Mac Neal* and *Harder* [57]. We then present the results for composite shell problems.

5.1. The hemispherical shell

The hemispherical shell ($R/h = 250$) presented in Fig. 7 is often used to evaluate the performance of a thin shell. This problem is introduced to prove the absence of membrane locking. On shell boundary, we impose free boundary conditions, except at 4-points under concentrated loads. Only a quarter of the structure is considered due to symmetry. The deflection values under concentrated loads are equal and opposite, $U_A = -V_B$, are presented in Table 2 and Fig. 8. The chosen quarter *ABCD* is divided with $N \times N \times 2$ for triangular elements and $N \times N$ for quadrilateral elements. The Symmetry conditions are $V = \theta_X = \theta_Z = 0$ on the side *AC*; $U = \theta_Y = \theta_Z = 0$ on the side *BC*. While the Boundary conditions are $W = 0$ at point *C*. In this problem, we use $R = 10\ m$; $h = 0.04\ m$; $R/h = 250$; $P = 1\ N$; $E = 6.825 \times 10^7 Pa$; $\upsilon = 0.3$. The reference solution is $U_A = -V_B = 0.094$ m.

Based on classical shell theory, the reference value is $U_A = 0.094\ m$. From Table 2 and Fig. 8, we found that DKMT18 element converges slightly faster than MITC4 element. The proposed shell element also gives better result, closer to the reference value.

5.2. Scordelis–Lo roof problem

The shell structures presented in Fig. 9 is a benchmark problem which is used to compare the shell element performance between flat facet approach and curved isoparametric shell. A quarter of the structure is used in the computation. Chosen cylindrical shell geometry and mechanical characteristics are defined in Fig. 9. One-quarter *ABCD* is discretized with $N \times N \times 2$ for triangular elements and $N \times N$ for quadrilateral elements. This shell is loaded by dead load applied as vertical load $f_z = -0{,}625 \times 10^4\ Pa$ distributed across the surface. In this test $L = 6\ m$; $R = 3\ m$; $h = 0.03\ m$; $\phi = 40^o$; $E = 3 \times 10^{10} Pa$ and $\upsilon = 0$ are evaluated. The Boundary condition are $U = W = \theta_Y = 0$ on the side *AD* while the Symmetry condition are $U = \theta_Y = \theta_Z = 0$ on the side *CD* and $V = \theta_X = \theta_Z = 0$ on the side *CB*. Reference value (theory of deep shell) is $W_B = -3.61\ cm$ and $W_C = 0.541\ cm$ and Analytical solution (theory of shallow shell): $W_B = -3.703\ cm$ and $W_C = 0.525\ cm$ [58].

Tables 3 and 4, and Figs. 10 and 11 present the results of the numerical test for DKMT18, DKMQ24, and MITC4 elements. We found that the DKMT18 element converges with a lower rate, but it gives close results to DKMQ24 and MITC4 starting from $N = 32$.

5.3. Pinched cylindrical shell with end diaphragms

The shell presented in Fig. 12 is a pinched cylinder loaded with two concentrated loads applied in the middle of the span in the opposite direction. At both ends of the cylinder, there is a rigid diaphragm that produces is a localized deflection around applied point load. Giving a complex deformation pattern where the bending effect dominates the structure under concentrated load, the example is a difficult test for the shell element. One-quarter of the shell is discretized with $N \times N \times 2$ for triangular elements and $N \times N$ for quadrilateral elements.

Data: $L = 6\ m$; $R = 3\ m$; $h = 0.03\ m$ and $0.3\ m$; $\upsilon = 0{,}3$; $E = 3 \times 10^{10}\ Pa$

Boundary condition: $U = W = \theta_Y = 0$ on the side *AD*

Symmetry conditions: $W = \theta_Y = \theta_X = 0$ on the side *AB*; $V = \theta_X = \theta_Z = 0$ on the side *BC*; $U = \theta_Y = \theta_Z = 0$ on the side *CD*

We consider two cases:

Case 1. *Reference value* ($R/h = 100$); $\underline{W_C} = Eh\ W_C/P = -164.24$

Case 2. *Reference value* ($R/h = 10$); $\underline{W_C} = Eh\ W_C/P = -11.351$

In this case, DKMT18 and DKMQ24 element provide much better results than the MITC4 element, which is due to a more precise quadratic interpolation for the rotation field used in DKMT18 and DKMQ24, which is superior to the MITC4 element, which uses linear interpolation functions. The results are computed for $R/h = 100$ and $R/h = 10$. For $R/h = 100$, an analytical solution was proposed by *Lindberg* et al. [59] or *Flügge* [60], obtained by the Fourier series. For $R/h = 10$, the

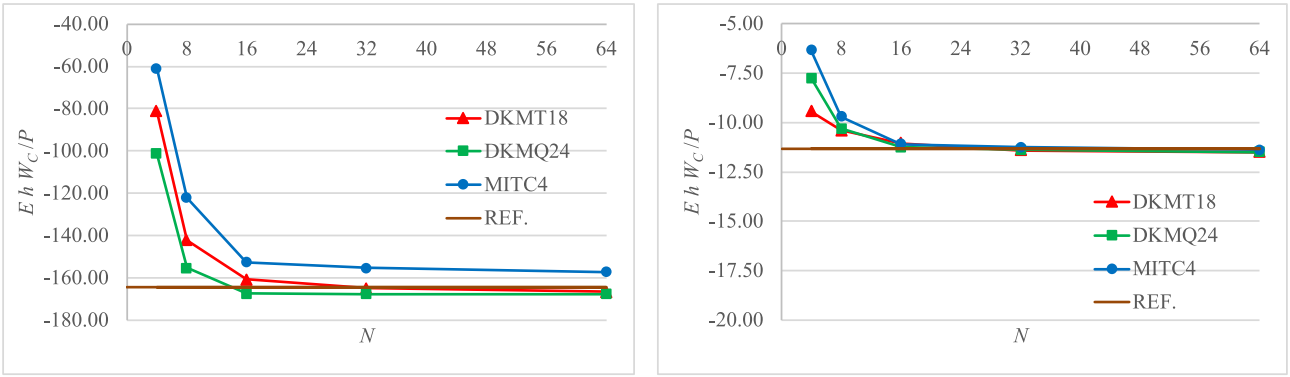

a. $R/h = 100$ *b.* $R/h = 10$

Fig. 13. Convergence of deflection $\underline{W_C}$.

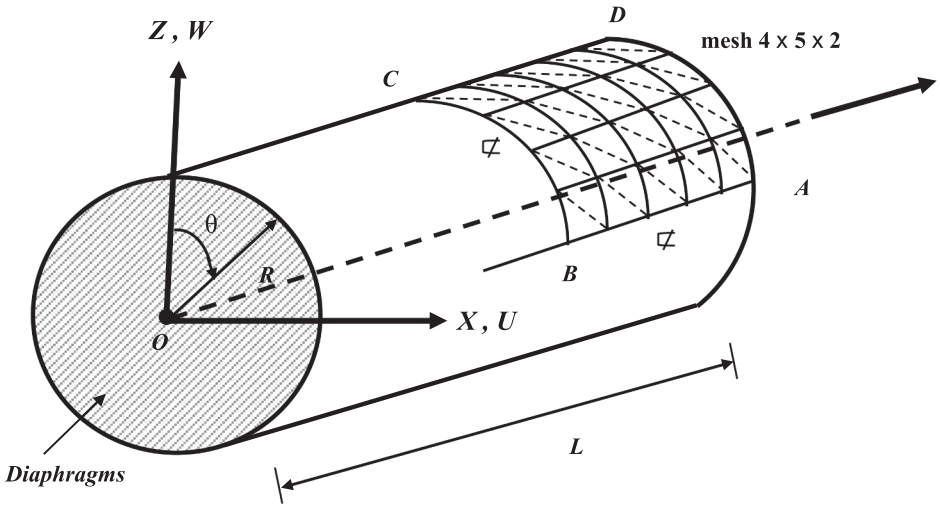

Fig. 14. Three-layered cylindrical shell.

Table 6
Convergence of central deflection $\underline{W_C}$ 3-layered cylindrical shell ($R/h = 50$).

$N \times M$	$R/h = 50$		
	DKMT18	DKMQ24	MITC4
4 × 5	0.4739	0.4411	0.3411
8 × 10	0.5229	0.5156	0.4909
16 × 20	0.5411	0.5380	0.5319
32 × 40	0.5446	0.5439	0.5423
64 × 80	0.5467	0.5464	0.5461
REF [63]	0.5495		

Table 7
Convergence of central deflection $\underline{W_C}$ 3-layered cylindrical shell ($R/h = 100$ and $R/h = 500$).

$N \times M$	$R/h = 100$		
	DKMT18	DKMQ24	MITC4
4 × 5	0.3873	0.3766	0.2957
8 × 10	0.4468	0.4447	0.4247
16 × 20	0.4653	0.4647	0.4598
32 × 40	0.4704	0.4700	0.4687
64 × 80	0.4712	0.4714	0.4611
REF [63]	0.4715		
$N \times M$	$R/h = 500$		
	DKMT18	DKMQ24	MITC4
4 × 5	0.0607	0.0779	0.0736
8 × 10	0.0899	0.0960	0.0950
16 × 20	0.0993	0.1011	0.1008
32 × 40	0.1019	0.1023	0.1023
64 × 80	0.1024	0.1026	0.1026
REF [63]	0.1027		

analytical solutions are presented in *Bhaskar* and *Varadan* [61]. In each of these two cases, only 1/8 of the cylinder is used for computations, accounting for the symmetries.

The numerical results for vertical displacement W_C for $R/h = 100$ and 10, are presented in Tables 5 and Fig. 13. We found that DKMT18 and DKMQ24 elements converge much faster than the MITC4 element.

5.4. Three–layer and Ten-layer cylindrical shell with sinusoidal pressure

A 3-layer and 10-layer cylindrical shell with sinusoidal pressure are

Table 8
Convergence of central deflection $\underline{W_C}$ 10-layered cylindrical shell ($R/h = 10$ and $R/h = 50$).

$N \times M$	$R/h = 10$			
	DKMT18	DKMQ24	MITC4	DKT18
4 × 5	1.2211	1.2158	1.0531	0.8108
8 × 10	1.2880	1.3046	1.2645	0.7971
16 × 20	1.3278	1.3381	1.3279	0.7966
32 × 40	1.3425	1.3469	1.3441	0.7965
64 × 80	1.3668	1.3636	1.3628	0.8130
REF [63]	1.3800			
$N \times M$	$R/h = 50$			
	DKMT18	DKMQ24	MITC4	DKT18
4 × 5	0.6302	0.6178	0.4778	0.6195
8 × 10	0.7228	0.7235	0.6885	0.7088
16 × 20	0.7534	0.7548	0.7461	0.7369
32 × 40	0.7618	0.7629	0.7607	0.7439
64 × 80	0.7687	0.7678	0.7673	0.7469
REF [63]	0.7622			

Table 9
Convergence of central deflection $\underline{W_C}$ 10-layered cylindrical shell ($R/h = 100$ and $R/h = 500$).

$N \times M$	$R/h = 100$			
	DKMT18	DKMQ24	MITC4	DKT18
4 × 5	0.4826	0.4983	0.3983	0.4811
8 × 10	0.5853	0.5917	0.5669	0.5832
16 × 20	0.6167	0.6188	0.6126	0.6142
32 × 40	0.6250	0.6258	0.6242	0.6221
64 × 80	0.6269	0.6274	0.6271	0.6238
REF [63]	0.6261			
$N \times M$	$R/h = 500$			
	DKMT18	DKMQ24	MITC4	DKT18
4 × 5	0.0578	0.0755	0.0721	0.0578
8 × 10	0.0872	0.0938	0.0927	0.0872
16 × 20	0.0970	0.0989	0.0983	0.0970
2 × 40	0.0997	0.1002	0.0997	0.0997
64 × 80	0.1002	0.1005	0.0992	0.1002
REF [63]	0.1006			

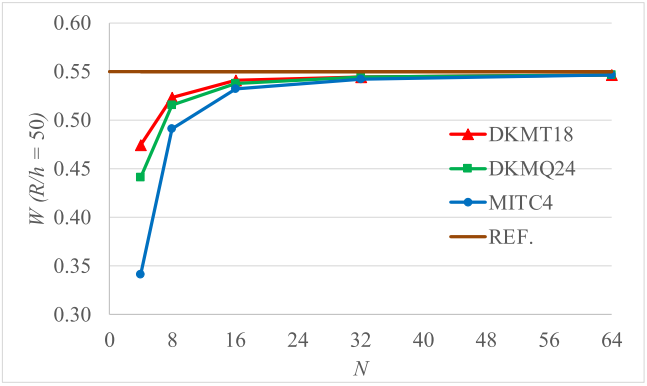

Fig. 15. Convergence of central deflection $\underline{W_C}$ of 3-layered cylindrical shell ($R/h = 50$).

analyzed. Due to symmetry condition, only one quarter of the shell is evaluated, as shown in Fig. 14. This test was earlier proposed as the benchmark by Ren [62], and then revisited by Varadan et Bhaskar [63], who provide the analytic solution. The details of this test are internal sinusoidal loading $Q = f_0 \sin(\pi Y/L) \cos(4\theta)$; 3-layered 90/0/90 and 10-layered $(90/0/90/0/90)_s$; $L = 80$ m; $R = 20$ m; $E_L = 25$ MPa; $E_T = 1$ MPa ; $\upsilon_{LT} = 0.25$; $G_{LT} = 0.5$ MPa; $G_{TZ} = 0.2$ MPa. The boundary condition: $U = W = \theta_Y = 0$ on the side AD and the symmetry conditions: $W = \theta_Y = \theta_X = 0$ on the side AB ; $V = \theta_X = \theta_Z = 0$ on the side BC; $U = \theta_Y = \theta_Z = 0$ on the side CD.

The reference value of central displacement is given by [63]:

$$\underline{W}_C = \frac{10E_L}{f_0 S^4 h} W_C \; ; S = \left(\frac{R}{h}\right)$$

Tables 6–9 and Figs. 15–18 show the comparison of the DKMT18 element with DKMQ24 and MITC4 elements for different ratios of R/h.

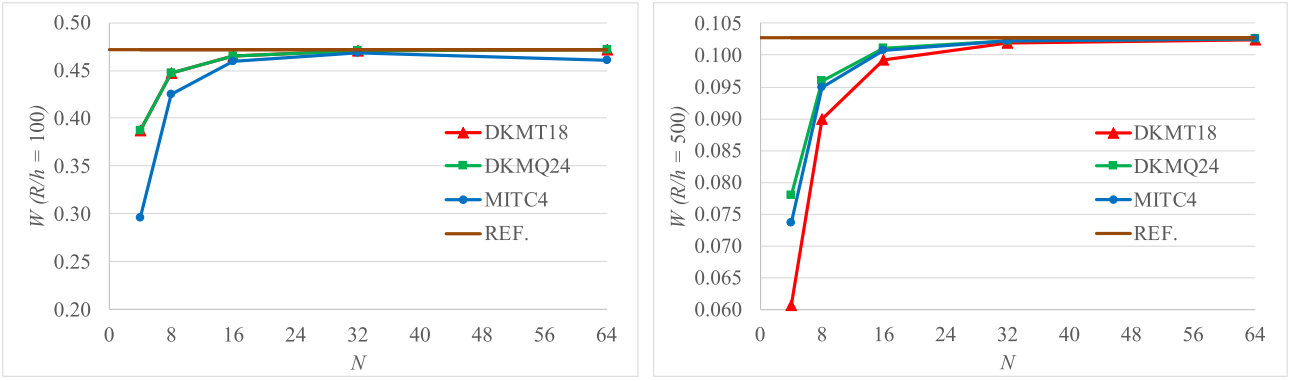

Fig. 16. Convergence of central deflection $\underline{W_C}$ of 3-layered cylindrical shell ($R/h = 100$ and $R/h = 500$).

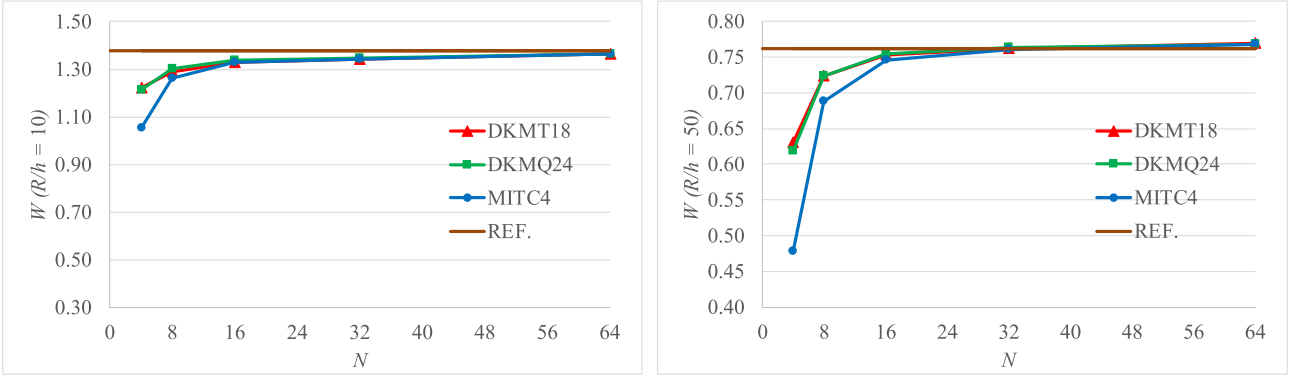

Fig. 17. Convergence of central deflection $\underline{W_C}$ of 10-layered cylindrical shell ($R/h = 10$ and $R/h = 50$).

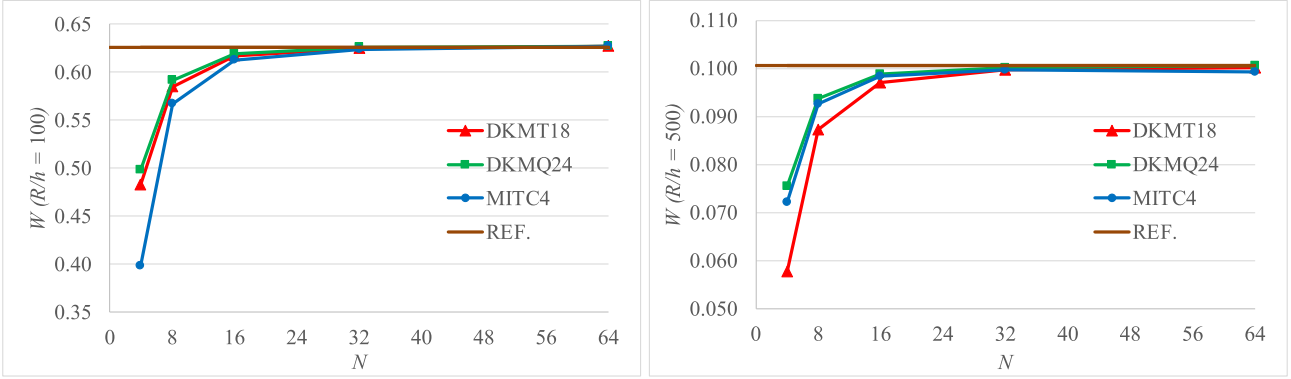

Fig. 18. Convergence of central deflection $\underline{W_C}$ of 10-layered cylindrical shell ($R/h = 100$ and $R/h = 500$).

In this case, we discretized $N \times M \times 2$ for triangular elements and $N \times M$ for quadrilateral elements. For the 3-layered 90/0/90 case, the three elements give very good results compared to the reference solution. We can see that DKMT18 and DKMQ24 elements converge faster than the MITC4 element for $R/h = 50$ and 100. While for $R/h = 500$, the DKMT18 element converges with a lower rate.

For the 10-layered case, as presented in Tables 8 and 9 and Figs. 17 and 18, once again, we found that DKMT18 and DKMQ24 elements converge faster than the MITC4 element. In Tables 8 and 9, the results for the DKT18 element are presented to see the contributions of transverse shear effects. For $R/h = 10$, the DKT18 element converges to another value due to the absence of transverse shear effects in the formulation of the element. When $R/h = 50$ and $R/h = 100$, as the contributions of transverse shear effects are smaller, the results of the DKT18 element become closer to the reference solution. We found the same results for DKMT18 and DKT18 when $R/h = 500$, where the contributions of transverse shear effects are neglected.

6. Conclusions

The presented DKMT18 shell element is a new three nodes with 18 DOFs. This element uses an incomplete quadratic interpolation for the rotation field, capable of dealing with both thick and thin isotropic and composite shell problems.

DKMT18 element is capable of equally reproducing the behavior of both the theory of the Kirchhoff and the Reissner-Mindlin, due to the use of a shear influence factor ϕ_k, which is a function of shell thickness ratio, which also explains the favorable position of the DKMT18 element relative to the MITC3 and DKT18 shell elements [46]. The DKMT18 element will become identical to the MITC3 element when ϕ_k become very big. On the other hand, the DKMT18 element become identical to the DKT18 element when ϕ_k become very small.

The numerical results show that this element can pass all standard validation tests, without shear locking as the DKMT plate element [39]. In bending dominated problems, results obtained with the DKMT18 element are excellent, and the convergence is much faster than with MITC4. These are due to the quadratic interpolation functions for the rotations used in DKMT18. For composite structures, the DKMT18 element also gives a good performance and provides results close to the reference solution. So, we can use the DKMT18 element as an alternative formulation in analyzing isotropic and composite structures.

CRediT authorship contribution statement

Imam Jauhari Maknun: Conceptualization, Writing - original draft, Software, Validation, Formal analysis. **Irwan Katili:** Conceptualization, Methodology, Writing - original draft, Supervision. **Adnan Ibrahimbegovic:** Writing - review & editing, Supervision. **Andi Makarim Katili:** Software, Validation.

Declaration of Competing Interest

The authors declare that they have no known competing financial interests or personal relationships that could have appeared to influence the work reported in this paper.

Acknowledgments

The authors gratefully acknowledge research grant from Universitas Indonesia, Indonesia, under Q1Q2 International Journal Publication Program (No: NKB-0303/UN2.R3.1/HKP.05.00/2019 and mobility grant from the Ministry of Research, Technology, and Higher Education (RISTEKDIKTI), Indonesia, through the PAR-WCU program (No: 311.28/D2.3/KP/2018).

References

[1] Oñate E. Structural analysis with the finite element method linear statics. Vol. 2 Beams, plates and shells. Springer; 2013.
[2] Naghdi PM. On the theory of thin elastic shells. Q Appl Math 1957;14:369–80.
[3] Naghdi PM. Foundations of elastic shells theory. In: Sneddon IN, Hill R, editors. Progress in solid mechanics; IV, Chapter 1. 1963. North-Holland.
[4] Naghdi PM. On a variational theorem in elasticity and its application to shell theory. J. Appl. Mech. (ASME) 1964;31(4):647–53.
[5] Naghdi PM. The theory of shells and plate. Handbuch der Physik, VI, A2 (Flugge Ed.). Berlin: Springer Verlag; 1972.
[6] Reissner E. The effect of transverse shear deformation on the bending of elastic plates. J Appl Mech Eng ASME 1945;12:A69–77.
[7] Mindlin RD. Influence of rotator inertia and shear on flexural motion of isotropic elastic plates. J Appl Mech Eng 1941;18:31–8.
[8] Hughes TJR. The finite element method: linear static and dynamic finite element analysis. Dover Publications Inc.; 2000.
[9] Belytschko T, Liu W, Moran B. Nonlinear finite elements for continua and structures. John Wiley & Sons Ltd.; 2000.
[10] Batoz J-L, Dhatt G. Modélisation des structures par éléments finis: Poutres et Plaques, vol. 2. Hermes Science Publications; 1990.
[11] Batoz J-L, Dhatt G. Modélisation des structures par éléments finis: Coques, vol. 3. Hermes Science Publications; 1992.
[12] Pawsey S, Clough R. Improved numerical integration of thick shell finite elements. Int J Numer Meth Eng 1971;3:575–86.
[13] Zienkiewicz O, Taylor R, Too J. Reduced integration technique in general analysis of plates and shells. Int J Numer Meth Eng 1974;3:275–90.
[14] Belytschko T, Ong J-J, Liu W, Kenedy J. Hourglass control in linear and non-linear problems. Comput Meth Appl Mech Eng 1984;43:251–76.
[15] Hughes TJR, Cohen M, Haroun M. Reduced and selective integration techniques in the finite element analysis of plates. Nucl Eng Des 1978;46:203–22.
[16] Hughes TJR, Taylor R, Kanoknukulchai W. A simple and efficient finite element for plate bending. Int J Numer Meth Eng 1977;11:1529–43.
[17] Malkus D, Hughes TJR. Mixed finite element methods-reduced and selective integration techniques: a unification of concepts. Comput Meth Appl Mech Eng 1978;15:63–81.
[18] Prathap G, Bhashyam G. Reduced integration and the shear-flexible beam element. Int J Numer Meth Eng 1982;18:172–8.
[19] Prathap G. The finite element method in structural mechanics. Dordrecht: Kluwer Academic Press; 1993.
[20] Stolarski H, Belytschko T. Membrane locking and reduced integration for curved element. J Appl Mech 1982;49:172–8.
[21] Adam C, Bouabdallah S, Zarroug M, Maitournam H. Improved numerical integration for locking treatment in isogeometric structural elements, Part I: Beams. Comput Meth Appl Mech Eng 2014;279:1–28.
[22] Adam C, Bouabdallah S, Zarroug M, Maitournam H. Improved numerical integration for locking treatment in isogeometric structural elements. Part II: Plates and shells. Comput Meth Appl Mech Eng 2015;284:106–37.
[23] MacNeal RH. Derivation of element stiffness matrices by assumed strain distributions. Nucl Eng Des 1982;70:3–12.
[24] Simo J, Rifai S. A class of mixed assumed strain methods and the method of incompatible modes. Int J Numer Meth Eng 1990;29:1595–638.
[25] Koschnick F, Bischoff M, Camprubi N, Bletzinger K-U. The discrete strain gap method and membrane locking. Comput Meth Appl Mech Eng 2005;194:2444–63.
[26] Hughes TJR, Taylor RL. The linear triangle bending elements. In the mathematics of finite element and application IV, MAFELAP. London: Academic Press; 1982. p. 127–42.
[27] Dvorkin EN, Bathe KJ. A continuum mechanics based four-node shell elements for general non-linear analysis. Eng Comput 1984;1:77–88.
[28] Lee PS, Bathe KJ. Development of MITC isotropic triangular shell finite elements. Comput Struct 2004;82(11):945–62.
[29] Lee Y, Lee PS, Bathe KJ. The MITC3+ shell element and its performance. Comput Struct 2014;138:12–23.
[30] Ko Y, Lee PS, Bathe KJ. A new MITC4+ shell element. Comput Struct 2017;182:404–18.
[31] Batoz J-L, Bathe KJ, Ho LW. A study of three-node triangular plate bending elements. Int J Numer Meth Eng 1980;15:1771–812.
[32] Batoz J-L, Ben Tahar M. Evaluation of a new thin plate quadrilateral element. Int J Numer Meth Eng 1982;18:1655–78.
[33] Batoz J-L, Lardeur P. A discrete shear triangular nine DOF element for the analysis of thick to very thin plates. Int J Numer Meth Eng 1989;28:533–60.
[34] Lardeur P, "Développement et evaluation de deux nouveaux éléments finis de plaques et coques composites avec influences du cisaillement transverse", Thèse de Doctorat, Université de Technologie Compiègne, France; 1990.
[35] Batoz J-L, Katili I. On a simple triangular Reissner/Mindlin plate element based on incompatible modes and discrete constraints. Int J Numer Meth Eng 1992;35:1603–32.
[36] Ibrahimbegović A. Plate quadrilateral finite element with incompatible modes. Commun Appl Numer Meth 1992;8:497–504.
[37] Ibrahimbegović A. Quadrilateral finite elements for analysis of thick and thin plates. Comput Methods Appl Mech Eng 1993;110:195–209.
[38] Ibrahimbegović A, Frey F. Stress resultant geometrically non-linear shell theory with drilling rotations. Part III: linearized kinematics. Int J Numer Meth Eng 1994;37:3659–83.
[39] Katili I. A new discrete Kirchhoff-Mindlin element based on Mindlin-Reissner plate

theory and assumed shear strain fields – part I: an extended DKT element for thick-plate bending analysis. Int J Numer Meth Eng 1993;36:1859–83.
[40] Katili I. A new discrete Kirchhoff-Mindlin element based on Mindlin-Reissner plate theory and assumed shear strain fields – part II: an extended DKQ element for thick plate bending analysis. Int J Numer Meth Eng 1993;36:1885–908.
[41] Mahjudin M, Lardeur P, Druesne F, Katili I. Stochastic finite element analysis of plates with the certain generalized stresses method. Struct Saf 2016;61:12–21.
[42] Wong FT, Erwin Richard A, Katili I. Development of the DKMQ element for buckling analysis of shear-deformable plate bending. Procedia Eng 2017;171:805–12.
[43] Katili I, Batoz JL, Maknun IJ, Lardeur P. A comparative formulation of DKMQ, DSQ and MITC4 quadrilateral plate elements with new numerical results based on s-norm tests. Comput. Struct 2018;204:48–64.
[44] Katili I, Maknun IJ, Millet O, Hamdouni A. Application of DKMQ element for composite plate bending structures. Compos Struct 2015;132:166–74.
[45] Maknun IJ, Katili I, Purnomo H. Development of DKMT element for error estimation in composite plate structures. Int J Technol 2015;6(5):780–9.
[46] Katili I, Maknun IJ, Batoz J-L, Katili AM. Asymptotic equivalence of DKMT and MITC3 elements for thick composite plate. Compos Struct 2018;206:363–79.
[47] Katili I, Batoz J-L, Maknun IJ, Hamdouni A, Millet O. The development of DKMQ plate bending element for thick to thin shell analysis based on Naghdi/Reissner/Mindlin shell theory. Finite Elem Anal Des 2014;100:12–27.
[48] Maknun IJ, Katili I, Millet O, Hamdouni A. Application of DKMQ24 shell element for twist of thin-walled beams: comparison with Vlasov theory. Int J Comput Methods Eng Sci Mech 2016;17(6):391–400.
[49] Irpanni H, Katili I, Maknun IJ. Development DKMQ shell element with five degrees of freedom per nodal. Int J Mech Eng Robot Res 2017;6:248–52.
[50] Katili I, Maknun IJ, Batoz J-L, Ibrahimbegović A. Shear deformable shell element DKMQ24 for composite structures. Compos Struct 2018;202:182–200.
[51] Katili I, Maknun IJ, Tjahjono E, Alisjahbana I. Error estimation for the DKMQ24 shell element using various recovery methods. Int J Technol 2017;6:1060–9.
[52] Katili AM, Maknun IJ, Katili I, "Theoretical equivalence and numerical performance of T3s and MITC3 plate finite elements", Struct Eng Mech, 69(5), 527-536.
[53] Katili I, Maknun IJ, Katili AM, Bordas SPA, Natarajan S. A unified polygonal locking-free thin/thick smoothed plate element. Compos Struct 2019;219:147–57.
[54] Katili I, Maknun IJ, Batoz J-L, Katili AM. A comparative formulation of T3γ_s, DST, DKMT and MITC3+ triangular plate elements with new numerical results based on s-norm tests. Eur J Mech A/Solids 2019;78:103826.
[55] Washizu K. Variational methods in elasticity and plasticity. 3rd ed. Pergamon Press; 1982.
[56] Ibrahimbegović A, Taylor RL, Wilson EL. A robust quadrilateral membrane finite element with drilling degrees of freedom. Int J Numer Meth Eng 1990;30:445–57.
[57] Mac Neal R, Harder RL. A proposed standard set of problems to test finite element accuracy. Finite Elem Anal Des 1985;1:3–20.
[58] Scordelis AC, Lo KS. Computer analysis of cylindrical shells. J Am Concr Inst 1969;61:539–62.
[59] Lindberg GM, Olson MD, Cowper GR, "New developments in finite element analysis of shells", Q. Bull. Div. Mech. Eng. and Nat. Aeronautical Establishment, National Research Council of Canada, Vol. 4; 1969.
[60] Flügge W. Stresses in shells. Springer Verlag; 1960.
[61] Bhaskar K, Varadan TK. Analytical solution for a pinched laminated cylinder. J Appl Mech (ASME) 1990;57:1082–3.
[62] Ren JG. Analysis of simply supported laminated circular cylindrical shell. Comput Struct 1989;11:277–92.
[63] Varadan TK, Bhaskar K. Bending of laminated orthotropic cylindrical shells – an elasticity approach. Compos Struct 1991;17:141–56.